Comput Mech (2011) 48:277–291
DOI 10.1007/s00466-011-0599-0

ORIGINAL PAPER

A comparison of outlet boundary treatments for prevention of backflow divergence with relevance to blood flow simulations

Mahdi Esmaily Moghadam · Yuri Bazilevs · Tain-Yen Hsia · Irene E. Vignon-Clementel · Alison L. Marsden · Modeling of Congenital Hearts Alliance (MOCHA)

Received: 12 March 2011 / Accepted: 30 March 2011 / Published online: 27 April 2011

Abstract Simulation divergence due to backflow is a common, but not fully addressed, problem in three-dimensional simulations of blood flow in the large vessels. Because backflow is a naturally occurring physiologic phenomenon, careful treatment is necessary to realistically model backflow without artificially altering the local flow dynamics. In this study, we quantitatively compare three available methods for treatment of outlets to prevent backflow divergence in finite element Navier–Stokes solvers. The methods examined are (1) adding a stabilization term to the boundary nodes formulation, (2) constraining the velocity to be normal to the outlet, and (3) using Lagrange multipliers to constrain the velocity profile at all or some of the outlets. A modification to the stabilization method is also discussed. Three model problems, a short and long cylinder with an expansion, a right-angle bend, and a patient-specific aorta model, are used to evaluate and quantitatively compare these methods. Detailed comparisons are made to evaluate robustness, stability characteristics, impact on local and global flow physics, computational cost, implementation effort, and ease-of-use. The results show that the stabilization method offers a promising alternative to previous methods, with reduced effect on both local and global hemodynamics, improved stability, little-to-no increase in computational cost, and elimination of the need for tunable parameters.

Keywords Neumann boundary conditions · Outflow stabilization · Lagrange multipliers · Normal velocity constraint · Patient-specific blood flow · Flow reversal · Navier–Stokes FEM solver · Cardiovascular simulation

MOCHA Investigators: Edward Bove MD and Adam Dorfman MD (University of Michigan, USA); Andrew Taylor MD, Alessandro Giardini MD, Sachin Khambadkone MD, Marc de Leval MD, Silvia Schievano PhD, and T-Y Hsia MD (Institute of Child Health, UK); G. Hamilton Baker MD and Anthony Hlavacek (Medical University of South Carolina, USA); Francesco Migliavacca PhD, Giancarlo Pennati PhD, and Gabriele Dubini PhD (Politecnico di Milano, Italy); Richard Figliola PhD and John McGregor PhD (Clemson University, USA); Alison Marsden PhD (University of California, San Diego, USA); Irene Vignon-Clementel (National Institute of Research in Informatics and Automation, France).

M. Esmaily Moghadam · A. L. Marsden
Mechanical and Aerospace Engineering Department, University of California, San Diego, USA

Y. Bazilevs (✉)
Structural Engineering Department, University of California, San Diego, USA
e-mail: jbazilevs@ucsd.edu

T.-Y. Hsia
Cardiac Unit, Institute of Child Health, Great Ormond Street Hospital for Children, London, UK

I. E. Vignon-Clementel
INRIA Paris-Rocquencourt, Rocquencourt, France

1 Introduction

The occurrence of backflow divergence is a well-known but not sufficiently addressed problem in the field of cardiovascular flow simulation. This problem usually arises in large vessels that are exposed to backflow in 3D and 2D flow simulations. There are three main situations that lead to numerical divergence caused by backflow. First, backflow divergence can result from bulk reversal of the flow through an outlet, such that there is negative flow over the entire outlet face. Second, there may be localized areas of flow reversal on an outlet face with bulk outward positive flow. And third, the use of multiscale modeling (e.g. using closed-loop lumped parameter 0D models [1,2], or 1D models [3–6] coupled to the 3D model) may necessitate the passing of pressure and

flow information for which there is a lack of velocity profile information, leading to numerical instabilities on either the coupled inflow or outflow faces. All of these numerical instabilities emanate from the use of Neumann boundary conditions on the outlet faces, for which velocity profile information is not specified [7–10].

Bulk backflow (complete flow reversal at an outlet) is a physiologic and commonly occurring phenomenon in the cardiovascular system in both healthy and diseased states. It often occurs in vessels during diastole and flow deceleration, particularly in certain regions. Thus, accurately capturing backflow phenomenon is essential for reproducing realistic conditions in many cardiovascular problems. Examples of physiologic flow reversal include flow in the descending abdominal aorta during diastole [11,5], flow reversal in the brachiocephalic artery after the stage 1 repair for single-ventricle heart patients (BT-shunt surgery) [12] and reversed flow due to respiratory effects in Fontan patients [13].

Backflow divergence due to local flow separation or flow recirculation is commonly caused by complex geometries such as the presence of stenoses, anastomoses, or increased cross sectional area, near the outlets of a model. These geometric features often lead to either steady or unsteady separation regions close to the outflow faces of a model, particularly at peak systolic flow. Similarly, geometric features can also lead to vortex shedding, and convection of vortices through the outflow faces, also leading to backflow divergence.

Multiscale modeling, in which a closed-loop lumped parameter network of ODEs is coupled to the inflow and outflow faces, usually requires Neumann boundary conditions on both inflows and outflows. In these situations, it is common that flow reversal is dictated by the pressure passed to the 3D model, causing a bulk inward flow without prescribing velocity profile information. In these situations, instabilities can occur, particularly in cases with rapidly changing dynamics that may alternate between positive and negative flow within a cardiac cycle. While we will not present results of multiscale modeling in this work, the exploration of outflow boundary treatments will set the stage for improved stability in coupled systems in future work.

Simulation divergence due to the above causes, for either total or partial flow reversal on an outlet face, requires careful consideration of the outflow boundary conditions. Since it is assumed that the inflow boundary condition is given, altering the inlet flow wave form to prevent backflow is not considered to be a viable solution [14,15]. Use of a mixed boundary condition [16,17], in which a Dirichlet boundary condition is used for the normal component of the velocity (either on the entire outlet or only in the region with backflow) along with a Neumann boundary condition for tangential velocity components, requires extra information about the velocity profile and the flow rate magnitude, which is generally unknown for the outlets.

The simplest solution to the backflow issue is to artificially elongate the outlets by adding long straight sections, thereby dissipating the vortices before they reach the outlet. While this has been commonly used in simulations [18–20] this method poses several major problems. First, it cannot be used as a solution for the case of total flow reversal at the outlet due to conservation of mass. Second, the addition of artificial extensions to the outlets has potential to change local hemodynamics, particularly in patient specific models or in multiscale modeling networks, where information as the boundary faces are coupled. And third, there is a non-negligible additional computational cost incurred by the need to mesh and simulate long outlet extensions. This added cost increases for high Reynolds number flows, since longer extensions will be needed to dissipate the vortices. Another option is to add additional vessels to the model until the flow becomes unidirectional and the Reynolds number at the outlet is reduced [21]. While this method has proven to be effective in patient-specific cases, it can only be used in a non-artificial way if the image resolution is adequate enough to permit inclusion of additional levels of branching. Additionally, this method increases the model generation and computational costs significantly. Due to these issues, we will not consider outlet extensions or additional branches as viable methods in the current work.

Apart from model extensions, there are three alternate methods currently in use for solving the issue of backflow divergence in finite element solvers.

1. Modifying the weak formulation by adding a backflow stabilization term for the Neumann boundaries [22].
2. Confining the backflow velocity to a desired direction, e.g. normal direction.
3. Using Lagrange multipliers for constraining the velocity profile to an assumed form [23].

The issue of backflow divergence has been addressed in previous work of Kim et al [23]. However, a thorough and quantitative comparison of these three methods using a single code has not been previously performed. In this paper we present a detailed comparison of these methods and compare their impact on the flow physics, computational cost, implementation effort, and robustness. The weak formulation is presented and then the modified formulation is discussed for each method. To produce an accurate comparison between the three methods, identical solver numerics, meshes, fluid properties, and inflow boundary conditions are used. The three backflow treatment methods are illustrated using three model problems which have relevance to blood flow simulation, as well as other internal flow problems in computational fluid dynamics, such as combustion simulations and duct flows.

First, a classic cylindrical expansion is studied with two exit lengths and two Reynolds numbers. This illustrates the case of backflow due to a localized steady separation region. Second, a 90-degree bend is studied with a physiologic unsteady inlet flow wave-form. This illustrates the case of backflow due to an asymmetric outlet velocity profile, as well as diastolic bulk flow reversal. The last case is a patient-specific model of an aorta, for which the untreated simulation diverges due to flow reversal during diastole. For this case, a non-ideal cut of an outlet is also considered to investigate the robustness of the proposed methods.

2 Methods

In this section, we present the numerical formulations of the three methods, based on previous work. The pros and cons of the three methods are as follows.

Outlet stabilization has been proposed by Bazilevs et al. [22] and used previously in cardiovascular applications. Advantages of this method include accuracy, robustness, ease of implementation, and little to no additional computational cost. Cons of the method are the potential to alter the local flow dynamics due to the addition of an artificial traction component opposite to the direction of the flow. However, as shown in the results section, these effects turn out to be minimal.

Confining the velocity profile to the normal direction is commonly used for stabilization in commercial flow solvers. While it has been effectively used in previous work, it has the obvious disadvantage of directly changing the local flow field if the assumed flow direction is not aligned with the flow. However, by choosing a proper direction, this method can cause little to no artifact in the flow field. The main disadvantages of this method are a lack of stability, as compared with the two other methods, which will be demonstrated in the results section.

Recent progress on backflow stabilization was made through the introduction of the Lagrange multiplier method for constraining the velocity profile of outlets. In the work of Kim et al. [23], this method was shown to have little effect on the local flow field, and effectively stabilize simulations that otherwise diverged. However, potential disadvantages of this method include complexity of implementation, the need for adjustable parameters, and significantly increased computational cost. Our work aims to build on this recent work by offering an alternative through the use of the stabilization method.

2.1 Governing equations

In this work, we consider the flow of an incompressible Newtonian fluid. Starting with the Navier–Stokes equations, the momentum and continuity equations can be written in index notation as,

$$\rho\dot{u}_i + \rho u_j u_{i,j} + p_{,i} - T_{ji,j} - f_i = 0,$$
$$\forall x \in \partial_g\Omega : u_i = g_i,$$
$$\forall x \in \partial_h\Omega : h_i = -pn_i + T_{ji}n_j, \tag{1}$$
$$u_{i,i} = 0. \tag{2}$$

where $\rho, u_i = u_i(x_i,t), \dot{u}_i = \dot{u}_i(x_i,t), p = p(x_i,t)$, $T_{ij} = T_{ij}(x_i,t)$ and $f_i = f_i(x_i,t)$ are the density, velocity vector, velocity time derivative taken with respect to a fixed spatial location, pressure, viscous stress tensor, and body forces vector, respectively. In Eq. (1), the Neumann and Dirichlet boundaries are denoted by $\partial_h\Omega$ and $\partial_g\Omega$, respectively. Defining the following operator

$$(f,g)_\Omega \equiv \int_\Omega f \cdot g \, d\Omega, \tag{3}$$

and denoting the velocity test function by w_i, the weak form of Eq. (1) is,

$$(w_i, \rho\dot{u}_i)_\Omega + \left(w_i, \rho u_j u_{i,j}\right)_\Omega + \left(w_i, p_{,i}\right)_\Omega - \left(w_i, T_{ji,j}\right)_\Omega - (w_i, f_i)_\Omega = 0. \tag{4}$$

Doing integration by parts for the pressure and viscous terms, we obtain

$$(w_i, \rho\dot{u}_i)_\Omega + \left(w_i, \rho u_j u_{i,j}\right)_\Omega - \left(w_{i,i}, p\right)_\Omega + \left(w_{i,j}, T_{ji}\right)_\Omega - (w_i, f_i)_\Omega + (w_i, pn_i)_{\partial_h\Omega} - \left(w_i, T_{ji}n_j\right)_{\partial_h\Omega} = 0, \tag{5}$$

where the $T_{ij} = \mu(u_{i,j} + u_{j,i})$ for Newtonian fluid. Considering q as the pressure test function, the continuity weak form can be obtained from Eq. (2) as,

$$\left(q, u_{i,i}\right)_\Omega = 0. \tag{6}$$

Finally the weak form is: Find $u_i \in \left\{u_i | u_i(x_i,t) \in (H^1)^d \times [0,T],\ u_i = g_i \text{ on } \partial_g\Omega\right\}$ and $p \in \left\{p | p(x_i,t) \in L^2 \times [0,T]\right\}$, such that for all $w_i \in \left\{w_i | w_i(x_i,t) \in (H^1)^d \times [0,T],\ w_i = 0 \text{ on } \partial_g\Omega\right\}$ and $q \in \left\{q | q(x_i,t) \in L^2 \times [0,T]\right\}$,

$$\begin{aligned} B(w_i,q;u_i,p) &= F(w_i,q) \\ B(w_i,q;u_i,p) &= (w_i,\rho\dot{u}_i)_\Omega + \left(w_i,\rho u_j u_{i,j}\right)_\Omega \\ &\quad - \left(w_{i,i},p\right)_\Omega + \left(w_{i,j},\mu u_{i,j}\right)_\Omega \\ &\quad + \left(w_{i,j},\mu u_{j,i}\right)_\Omega \\ &\quad - \left(q_{,i},u_i\right)_\Omega + (q,u_i n_i)_{\partial\Omega}, \\ F(w_i,q) &= (w_i,f_i)_\Omega + (w_i,h_i)_{\partial_h\Omega}. \end{aligned} \tag{7}$$

In the discrete setting, we make use of a stabilized formulation (see, e.g., [24–29]), which allows equal-order velocity and pressure interpolation, and addresses the convective instability associated with Galerkin's method applied to Eq. (7). The weak form in Eq. (7) is discretized in space with P1 finite elements, and in time using the Generalized-α method [30].

After discretization of Eq. (7) the residual vector can be obtained. Using the generalized-α method for time integration and the Newton–Raphson method to form the stiffness matrix we have,

$$\begin{bmatrix} \boldsymbol{K} & \boldsymbol{G} \\ \boldsymbol{D} & \boldsymbol{L} \end{bmatrix} \begin{bmatrix} \Delta \dot{\boldsymbol{U}} \\ \Delta \boldsymbol{P} \end{bmatrix} = \begin{bmatrix} -\boldsymbol{R}_m \\ -\boldsymbol{R}_c \end{bmatrix} \tag{8}$$

where $\boldsymbol{R}_m$ and $\boldsymbol{R}_c$ are the momentum and continuity residual vectors, respectively, and $\boldsymbol{K}$, $\boldsymbol{G}$, $\boldsymbol{D}$, and $\boldsymbol{L}$ matrices are defined by,

$$\begin{aligned} \boldsymbol{K} &= \frac{\partial \boldsymbol{R}_m}{\partial \dot{\boldsymbol{U}}^{n+1}}, \\ \boldsymbol{G} &= \frac{\partial \boldsymbol{R}_m}{\partial \boldsymbol{P}^{n+1}}, \\ \boldsymbol{D} &= \frac{\partial \boldsymbol{R}_c}{\partial \dot{\boldsymbol{U}}^{n+1}}, \\ \boldsymbol{L} &= \frac{\partial \boldsymbol{R}_c}{\partial \boldsymbol{P}^{n+1}}, \end{aligned} \tag{9}$$

where $\dot{\boldsymbol{U}}$ and $\boldsymbol{P}$ are vectors discretized in space, containing the time derivative of velocity and pressure, respectively. Superscript n denotes the time step and α_f and γ are generalized-α method parameters which are defined based on the spectral radius of infinite time step (for details see [30, 21]). This system is solved with a combination of a conjugate gradient method and a preconditioned Generalized Minimum Residual (GMRES) method. For more details about the discretization, linearization, and linear solvers, see [23,31].

2.2 Methods for backflow treatment

2.2.1 Outlet stabilization

In this section, we follow the implementation of Bazilevs et al. [22] for the addition of stabilization terms on the outflow boundaries. The weak form in Eq. (7) is vulnerable to backflow divergence. To obtain a more stable weak form in the regions with backflow, an additional convective traction is added. The parameter β presents a modification to the method proposed in [22]. The original formulation, presented in [22], is equivalent to the current formulation for $\beta = 1$. In this work, we present a modification of this method in which a fraction of this term is added, and a more stable method is obtained. From our numerical experience, this coefficient allows us to have a stable solution for larger time-step values compared to the $\beta = 1$ case, when there is significant flow reversal. The stabilization term can be defined as follows

$$\begin{aligned} \tilde{B}(w_i, q; u_i, p) = B(w_i, q; u_i, p) \\ -\beta \left(w_i, \rho (u_j n_j)_- u_i\right)_{\partial_h \Omega}, \end{aligned} \tag{10}$$

where β is a positive coefficient between 0.0 and 1.0. For small values of β, this method is less intrusive and also stable in numerical experiments over a larger range of time steps. In Eq. (10), $(u_i n_i)_-$ is defined as,

$$(u_i n_i)_- \equiv \frac{u_i n_i - |u_i n_i|}{2} = \begin{cases} u_i n_i & u_i n_i < 0 \\ 0 & u_i n_i \geq 0. \end{cases} \tag{11}$$

Considering the weak form of Eq. (10), since the $-\beta(u_j n_j) - (u_i, u_i)$ term is always positive, the energy dissipation added by this term is proportional to the degree of backflow velocity. In physical terms, the added term in Eq. (10) is an outward traction, opposite the direction of backflow, which pushes the flow in the direction of the outward normal. In this sense, this term provides the "missing" convective flow information from outside of the computational domain during flow reversal.

2.2.2 Normal velocity constraint

In this method, the velocity is constrained to be in a particular direction, e_i, which is usually set to the surface normal direction. Therefore, a zero Dirichlet velocity is imposed for the tangential directions. Although the normal velocity boundary condition formulation can be found in standard FEM text books [32], we have included the formulation here for the sake of completeness. The momentum equation of the outlet nodes is modified such that the two tangential velocity components are zero, but the momentum equation is unchanged in the normal direction. Let us define a rotation matrix $\boldsymbol{M}$ by,

$$\boldsymbol{M} = \begin{bmatrix} \boldsymbol{e} \\ \boldsymbol{t}_2 \\ \boldsymbol{t}_3 \end{bmatrix}, \tag{12}$$

where $\boldsymbol{t}_2$ and $\boldsymbol{t}_3$ are the directions orthogonal to the vector $\boldsymbol{e}$. To confine the velocity in the normal direction, $\boldsymbol{e}$, $\boldsymbol{t}_2$ and $\boldsymbol{t}_3$ in Eq. (12) are simply replaced by $\boldsymbol{n}$ and its orthogonal vectors. Multiplying Eq. (8) by $\boldsymbol{M}$ in the element level rotates it to the normal and tangential coordinates. From Eq. (8), for node B at the outlet surface we have

$$M_{ij} k_{jk}^{AB} M_{kl}^t M_{lp} \Delta \dot{U}_p^B + M_{ij} g_j^{AB} P^B = -M_{ij} r_{mj}^A, \tag{13}$$

where $\boldsymbol{k}$ and $\boldsymbol{g}$ are element stiffness matrices and $\boldsymbol{r}_m$ is the momentum element residual vector. To eliminate tangential components of $M_{ij} \Delta \dot{U}_j^B$, the stiffness matrices and residual vector are replaced by

$$\begin{aligned} \tilde{k}_{ij}^{AB} &= M_{\hat{i}k} k_{kl}^{\hat{A}\hat{B}} M_{l\hat{j}}^t \delta_{\hat{i}\hat{j}} \delta_{\hat{A}\hat{B}}, \\ \tilde{g}_i^{AB} &= M_{\hat{i}j} g_j^{\hat{A}\hat{B}} \delta_{\hat{i}1} \delta_{\hat{A}\hat{B}}, \\ \tilde{r}_{mi}^A &= M_{\hat{i}j} r_{mj}^A \delta_{\hat{i}1}. \end{aligned} \tag{14}$$

where δ_{ij} is the Kronecker's delta, equal to one for $i = j$ and zero for $i \neq j$. There is no summation over the indices with the hat notation, e.g. $\hat{i}$.

Substituting Eq. (14) into (13) and multiplying by $\boldsymbol{M}^t$ to rotate back to original coordinates, we have

$$M_{ij}^t \tilde{k}_{jk}^{AB} M_{kp} \Delta \dot{U}_p^B + M_{ij}^t \tilde{g}_j^{AB} P^B = -M_{ij}^t \tilde{r}_{mj}^A, \tag{15}$$

which can be rewritten as

$$\bar{k}_{ji}^{AB} \Delta \dot{U}_i^B + \bar{g}_j^{AB} P^B = -\bar{r}_{mj}^A : B \in \partial_h \Omega, \tag{16}$$

so that the modified stiffness matrices, $\bar{\boldsymbol{k}}$, $\bar{\boldsymbol{g}}$, and residual vector, $\bar{\boldsymbol{r}}_m$, are defined by

$$\begin{aligned} \bar{k}_{ij}^{AB} &= M_{ik}^t \tilde{k}_{kl}^{AB} M_{lj}, \\ \bar{g}_i^{AB} &= M_{ij}^t \tilde{g}_j^{AB}, \\ \bar{r}_{mi}^A &= M_{ij}^t \tilde{r}_{mj}^A. \end{aligned} \tag{17}$$

By using Eqs. 12–14 and 17, the modified element stiffness matrices and residuals are found from $\boldsymbol{k}$, $\boldsymbol{g}$ and $\boldsymbol{r}_m$ and can be assembled into the global matrices and vector. One might add another requirement of $U_i^B n_i^B < 0$ to Eq. (16), in order to only effect the nodes with inward velocity (i.e. defining this equation only on $\partial_{h\_} \Omega$). But for this study, we restrict all the nodes on the outlet surface to obtain a more stable and general form. It should be noted that while commercial solvers often have an option for normal velocity constraints, it is impossible to guarantee identical implementation since this information is typically proprietary.

2.2.3 Constraining the velocity profile

The concept of this method is to assume a particular velocity profile, e.g. parabolic, for the outlet and then constrain the solution to converge to this assumption. This is achieved by adding penalties to the residual vector for deviation from this assumption. To this end, the following constraints are enforced using the augmented Lagrange multiplier method as in the work of Kim et al. [23].

$$\begin{aligned} c_1 &= \alpha \left(u_i n_i - \phi, u_i n_i - \phi\right)_{\partial_h \Omega} = 0, \\ c_2 &= \alpha \left(u_i t_{2i}, u_i t_{2i}\right)_{\partial_h \Omega} = 0, \\ c_3 &= \alpha \left(u_i t_{3i}, u_i t_{3i}\right)_{\partial_h \Omega} = 0, \end{aligned} \tag{18}$$

where t_{2i} and t_{3i} are tangential surface vectors and $\phi(x_i, t)$ is the velocity profile to be imposed,

$$\phi = \frac{(u_i, n_i)_{\partial_h \Omega}}{(1, 1)_{\partial_h \Omega}} \frac{n+2}{n} \left(1 - \left(\frac{r}{R}\right)^n\right), \tag{19}$$

where n is the velocity profile polynomial order defined by the user, $r(x_i)$ is the distance from the center of the face, and R is the surface radius defined by the user. Also, α which is used to nondimensionalize Eq. (18) is,

$$\alpha = \frac{(1, 1)_{\partial_h \Omega}}{\bar{Q}^2}, \tag{20}$$

where $\bar{Q}$ is a user-defined estimate of the average flow rate through the surface. Note that the definition of Eq. (19) implies the requirement of circular outlet cross sections, although this is not strictly required for use in all problems.

Having c_i from Eq. (18), a weak form obtained from the following equation is included in the formulation for all the constrained surfaces (see [23]),

$$-\lambda_i c_i + \frac{1}{2} \kappa_i c_i^2 + \sigma_i \lambda_i^2 = 0, \tag{21}$$

where λ, κ, and σ are Lagrange multipliers (part of the solution vector), user-defined penalty numbers, and regularization parameters, respectively. The regularization parameters, which are chosen to be small, are used to prevent an ill-conditioned stiffness matrix.

2.3 Model construction and simulation methods

To create the geometric models, a customized in-house version of the open source Simvascular package was used [33]. Models for the first two cases were analytically defined and constructed by lofting together circles. For the patient-specific model in case three, starting from the X-ray computed tomography (CT scan), the geometry of each artery is identified and segmented [34]. By lofting these segments through the centerline of the vessels, the solid model is created. Then, the model is meshed with tetrahedral elements using the MeshSim© software package. A customized version of the finite element code, Phasta [33] (open sourced at simtk.org), is used for simulations. All simulations are done with rigid walls, incompressible, and Newtonian fluid assumptions. Blood density and viscosity are set to be 1,060 Kg/m^3 and 0.004 Pa · s. The spectral radius of infinite time step, so called ρ_∞, is set to 0.2 for all simulations. At the inlet, a Dirichlet velocity condition is imposed. At the outlet, when a zero traction Neumann boundary condition is imposed, all components of the traction are set to zero, i.e. $h_i = 0$ in Eq. (7). An implicit method (the coupled multi-domain method) is adopted for RCR outlet boundary conditions, in which the derivative of the imposed pressure at each time step is considered in the stiffness matrix [5,35]. The same number of non-linear iterations are used for all methods. All three methods for outflow treatment were implemented in the same code with identical numerics and meshing, allowing for an "apples-to-apples" comparison of the three methods. The implementation of the Lagrange method used in this work was done by Kim et al., and included in the open source release of the Simvascular package.

For all the case studies, the β value in Eq. (10) is equal to 0.2. The profile order, i.e. n in Eq. (19), is equal to 2 for all Lagrange cases, corresponding to a parabolic profile, unless stated otherwise. The penalty numbers, κ, are also set to 10^6, unless stated otherwise. Also, e_i is set to the surface normal

vector, n_i, in Eq. (12). A Dirichlet boundary condition is imposed at the inlet with a parabolic velocity profile in all cases.

3 Results

3.1 First case study

The first case study is a cylinder with an expansion, as shown in Fig. 1. The inlet and outlet diameters are 5 and 10 mm, respectively. The lengths of the inlet and expansion sections are 10 and 5 mm, respectively. Two lengths, 15 and 30 mm, are used for the outlet sections in the short and extended models, respectively. The short and extended models are meshed with 215, 910 and 320, 157 tetrahedral linear elements, respectively. The results are presented based on the inlet Reynolds number with a steady inflow rate. A zero traction boundary condition is imposed for the outlet. As shown in Fig. 2, the expansion in cross section produces a recirculation region which causes backflow at the outlet at high Reynolds numbers.

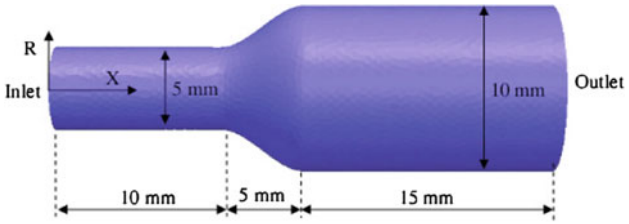

Fig. 1 Short solid model for first case study with 15 mm outlet section

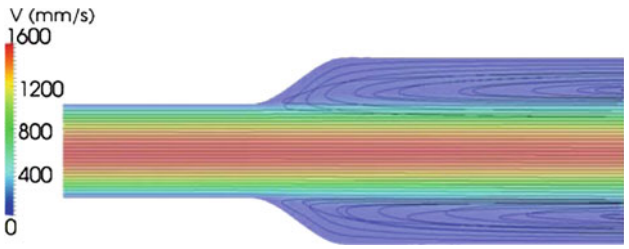

Fig. 2 Velocity contours and stream lines at Re = 1,000 for first case study illustrating stable vortices at the outflow face

3.1.1 Extended model

This simulation is done with the extended model and an inlet Reynolds number of 1,000. At this Reynolds number and model length there is a very small amount of backflow, and the simulation is stable with no boundary treatment. A comparison of simulation results is shown in Fig. 3 for the no boundary treatment case and the three treatment methods. The pressure and velocity at the centerline and the outlet are plotted in this figure.

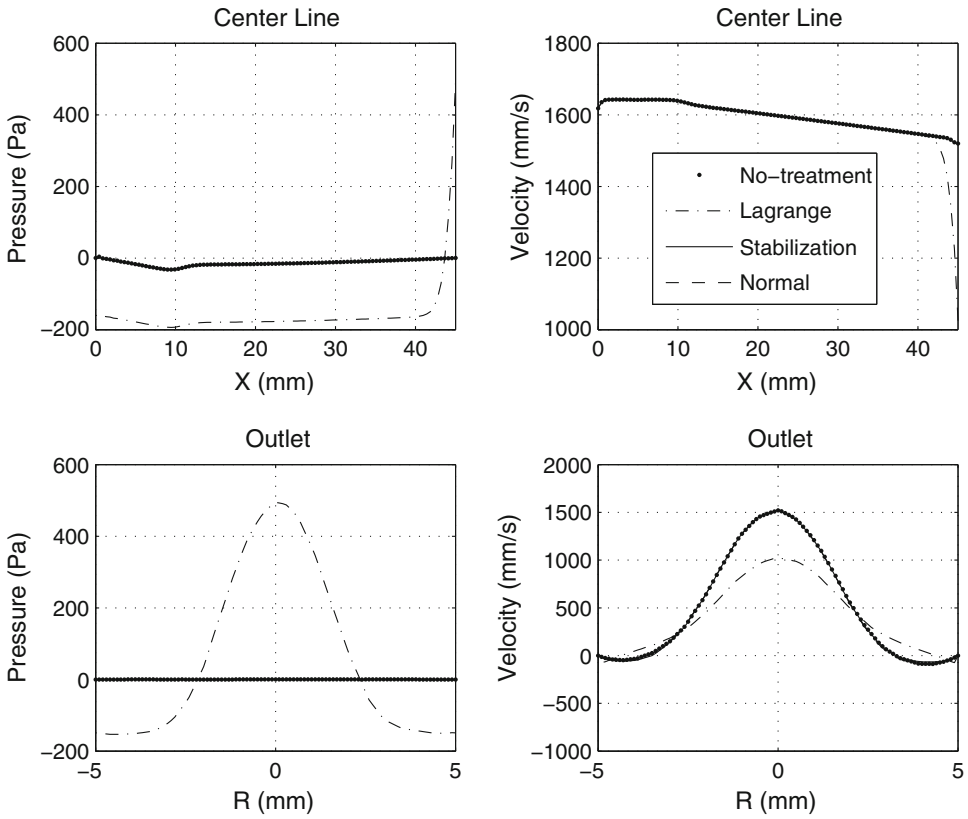

Fig. 3 Velocity and pressures for the extended model at the centerline and outlet section at Re = 1,000

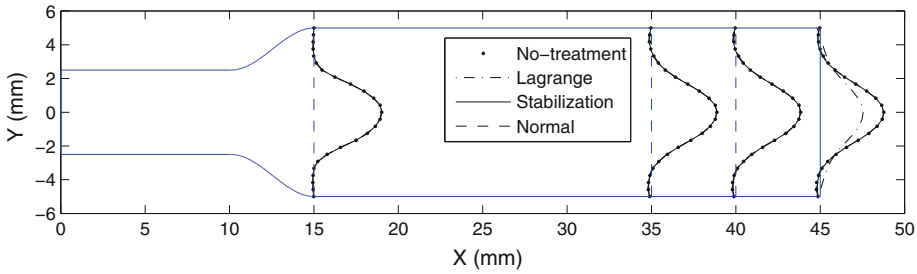

Fig. 4 Velocity profiles at $x = 15$, 35, 40 and 45 mm in the extended model at Re = 1,000

We observe that the stabilization and normal constraint method results are very close to the no-treatment case. However, the Lagrange method failed to match to the no-treatment case results. Although this method does not change the velocity in the region far from the outlet (see Fig. 4), the velocity profile is changed significantly at the outlet, as expected. The changes in the velocity profile at the outlet are responsible for changes in the outlet pressure as well. The reduction of velocity at the center and its increase in the peripheral region requires higher and lower pressure in those areas, respectively, to satisfy the momentum equations. This change in pressure is propagated throughout the model.

From Fig. 3 it is clear that the Lagrange method has a significant effect on the flow physics. To magnify the difference between the normal constraint and the stabilization method, deviation of these methods from the no-treatment case is shown in Fig. 5 as the percent error. This figure suggests that in this case the stabilization method has a larger impact on the flow than the normal constraint method. This may be a result of the added traction from the stabilization term, which opposes the inward flow.

To obtain a more global picture of the effect of these methods on the flow, the outlet and inlet energy fluxes and average pressures are tabulated (Table 1). Wall time is the parallel simulation time with 8 processors under the same circumstances for all cases. This table also confirms the results shown in Figs. 3 and 5. Comparing the stabilization and normal constraint methods, the normal constraint is slightly less intrusive, but more costly. The Lagrange method has the highest impact on the flow with highest computational cost. Use of a higher profile order in the Lagrange method slightly reduces the effect on the flow physics. The same is also true for lower penalty numbers, but this will also decrease the robustness of the method.

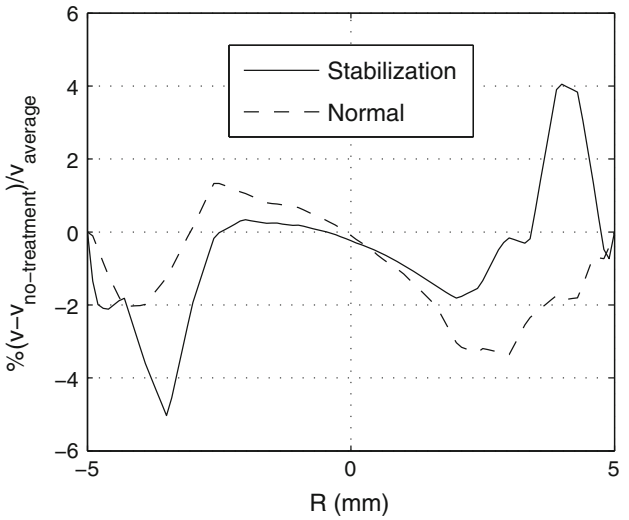

Fig. 5 Differences in velocity for the normal constraint and stabilization methods compared to no-treatment case at the outlet of the extended model at Re = 1,000

3.1.2 *Short model*

The short model with no treatment at a Reynolds number of 1,000 is not stable. The results shown in Fig. 6 are analogous to Fig. 3. The zero traction boundary condition is not satisfied for the Lagrange method. As expected, the outlet velocity profile for this method is closer to a parabolic profile.

Table 1 Comparison of the average pressure and energy fluxes for all methods with the extended model at Re = 1,000

Methods	Wall time (s)	$\bar{P}_{in}$ (Pa)	$\bar{P}_{out}$ (Pa)	$\dot{E}_{in}$ (mW)	$\dot{E}_{out}$ (mW)	$-\dot{E}_{out}/\dot{E}_{in}$ (%)
No-treatment	379	1.90	–0.029	–10.89	8.70	79.9
Stabilization	394	0.26	–0.32	–10.87	8.70	79.9
Normal	399	1.72	–0.284	–10.89	8.69	79.8
Lagrange	537	–160	–63.3	–8.36	5.48	65.6
Lagrange ($n = 5$)	532	–128	–30.4	–8.85	6.01	69.4
Lagrange ($\kappa = 10^5$)	523	–57.1	–26.6	–9.97	7.66	76.8

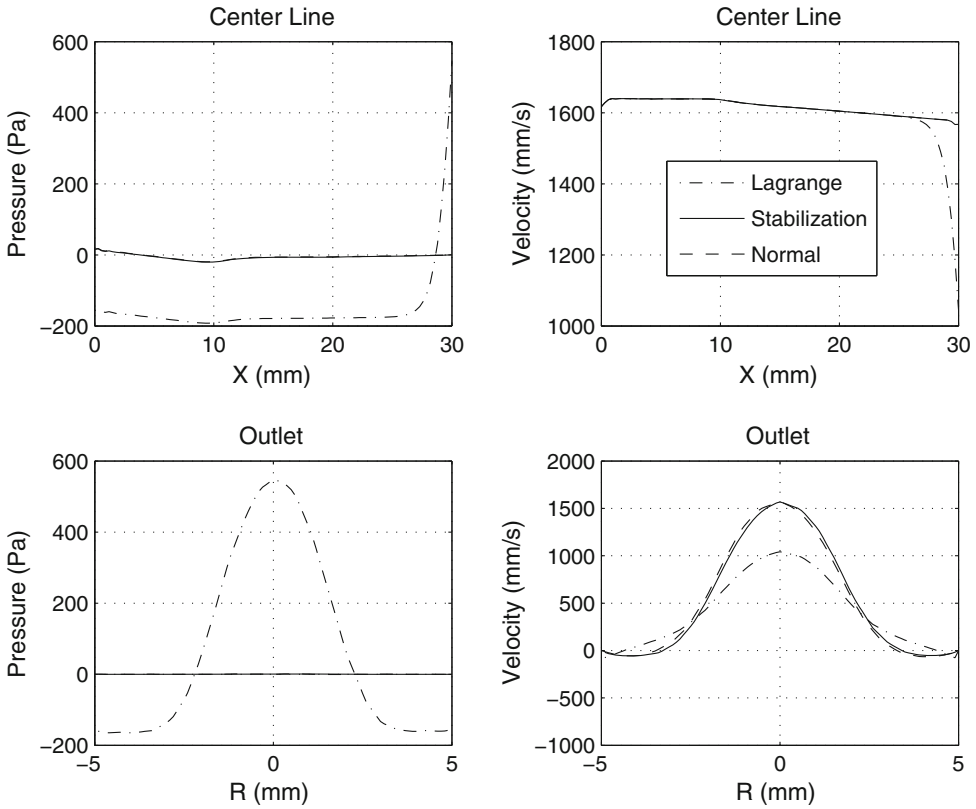

Fig. 6 Velocity and pressures for the short model at Re = 1,000

3.1.3 Higher Reynolds number

Figure 7 shows the results for the short model at a Reynolds number of 5,000. In this figure, the Lagrange method velocity results are closer to the other two. However, the pressure at the centerline is lower at the inlet and rapidly increases at the outlet. This suggests lower pressure energy dissipation in this method as compared with the others. To obtain stable results, the time-step size is reduced to 10^{-3} from 10^{-2} for the lower Reynolds number case. When increasing the Reynolds number further to 2×10^4, the Lagrange (keeping the penalty numbers and profile order unchanged) and normal constraint methods are no longer stable, where the stabilization method remains stable. For the stabilization method, we found that for lower β values, the solution was stable for higher time-step values.

Considering the centerline velocity at Re = 1,000 and 5,000 in Figs. 6 and 7, the impact of the both the stabilization and normal constraint methods on the centerline velocity increases with the Reynolds number. This can be inferred by the sharp reduction of the centerline velocity at the outlet at Re = 5,000. Also, the centerline pressure of these two methods does not match as well at Re = 5,000 as it does at Re = 1,000.

3.2 Second case study: right angle bend

The second example illustrates pulsatile flow through a right-angle bend. The radius of the bend centerline is 10 mm and its diameter is 5 mm. This is a common shape in the arterial system, e.g. in a child's descending aorta. This simulation is done with a time-step equal to 10^{-4} over 1 s with three nonlinear iterations per time-step. The inflow waveform is physiological, with a cardiac cycle time of 0.5 s [36]. This wave form (Q_1) and the model are shown in Fig. 8. The average flow rate was scaled to produce an average Re = 2,500. This high Reynolds number is chosen to challenge the robustness of these methods, and is above the normal physiologic range. However, high Reynolds number such as this can occur in the other applications, such as flow simulation through pipes and ducts. Analogous to the previous case, a zero traction boundary condition is set for the outlet. Both the normal constraint and the no-treatment cases were unstable.

From Table 2, the Lagrange method results show large differences in the inlet and outlet pressures compared to the stabilization method results. Similar to the previous cases, the zero traction boundary condition at the outlet is not satisfied for the Lagrange method. This is due to the added normal traction at the outlet, which increases the pressure

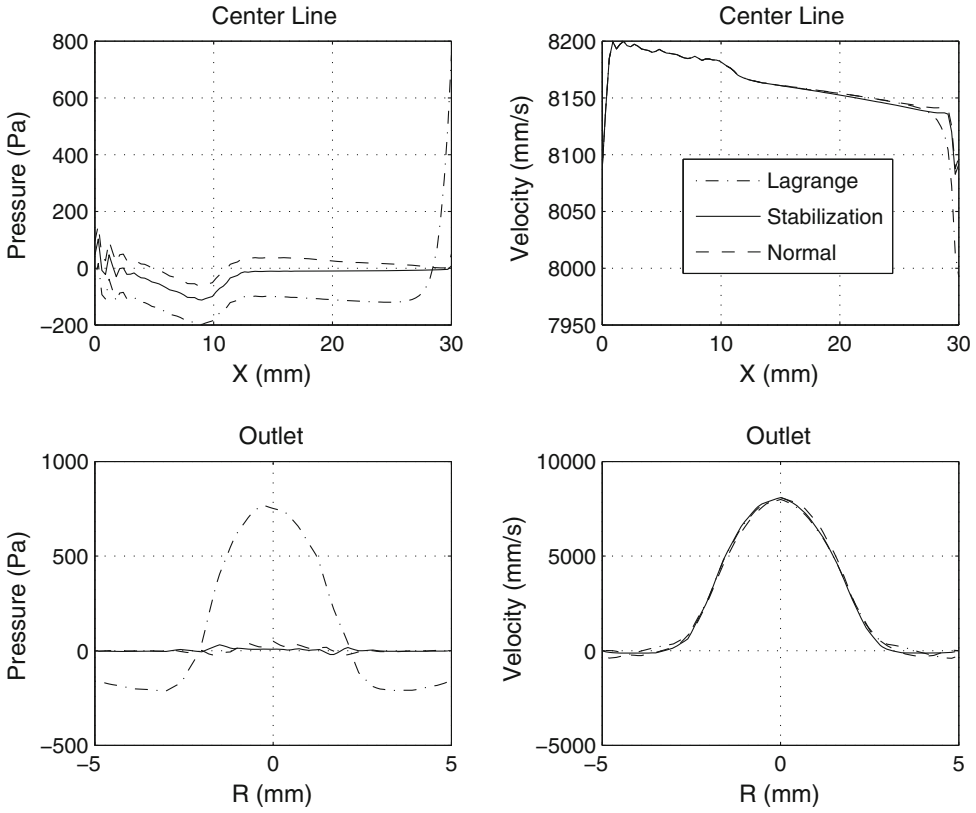

Fig. 7 Velocity and pressures for the short model at Re = 5,000

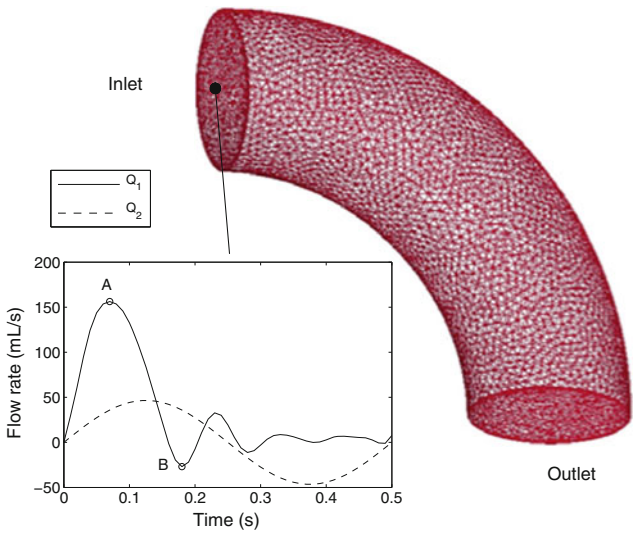

Fig. 8 Second case study geometric model and inflow waveforms

at the outlet nodes, for the Lagrange method. This pressure propagates through the model, causing higher pressure at the inlet as well.

The inflow wave form was changed to a more critical case of $\pi^2 D\nu \mathrm{Re} \sin(2\pi t/T)/8$, where the T, D, ν, and Re are one cycle period, inlet diameter, fluid kinematic viscosity, and average Reynolds number, respectively. This inflow wave form has more backflow, as shown by Q_2 in Fig. 8. The Reynolds number is set to 2,000. At this Reynolds number the normal constraint simulation diverged. The Lagrange constraint case remained stable, but the result was physically unrealistic, with a high pressure oscillation through the cardiac cycle. The stabilization method result, on the other hand, was stable and the solution residual was low.

Figure 9 illustrates the larger differences in the outlet velocity vector found using the Lagrange and stabilization methods. The vectors in Fig. 9b which are colored by pressure, clearly show the low artificial pressure at the center of the outlet which tends to increase the velocity at the center

Table 2 Comparison between the average pressure and energy fluxes of the curved model at average Re = 2,500 for case study two

Method	$\bar{P}_{in}$ (Pa)	$\bar{P}_{out}$ (Pa)	$\dot{E}_{in}$ (W)	$\dot{E}_{out}$ (W)	$-\dot{E}_{out}/\dot{E}_{in}$ (%)
Stabilization	1,192	–24.1	–1.585	1.372	86.5
Normal	–	–	–	–	–
Lagrange	1,781	433.7	–1.584	1.323	83.5

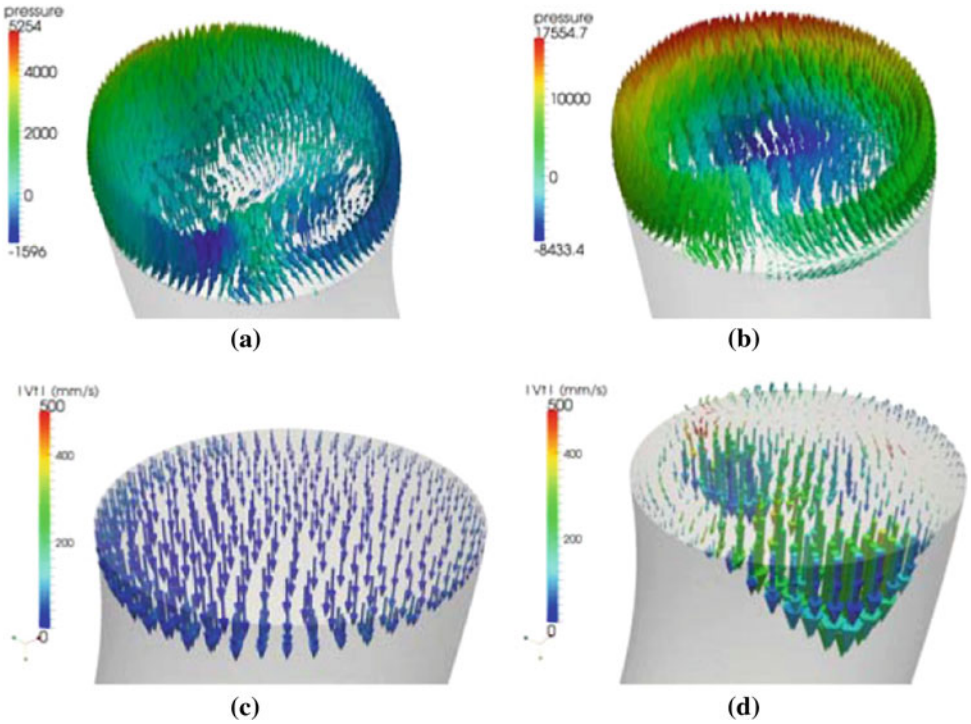

Fig. 9 Second case study, outlet velocity vectors at peak flow (point *A* in Fig. 8) colored by pressure (Pa) using **a** stabilization method and **b** Lagrange method; and velocity vectors after deceleration (point *B* in Fig. 8) colored by tangential velocity for **c** stabilization method and **d** Lagrange method

to achieve the desired parabolic profile. This is also true for the region of the outlet with high velocity close to the wall, which has a higher artificial pressure. The residual value is low for the stabilization method over the entire cycle, but the residual increases in diastole for the Lagrange method. This is the reason that after deceleration (i.e. point *B* in Fig. 8) the velocity vectors shown in (d) are inconsistent with part (c) of Fig. 9.

3.3 Third case study: a patient-specific aorta model

The final case study is an aortic arch model constructed from CT data of a healthy, 62-year old male patient, which is shown in Fig. 10. In addition to the aorta, three branches of the brachiocephalic artery, the left common carotid artery, and the left subclavian artery are included in the model. Physiologic RCR boundary conditions are imposed at all outlets [35,37]. The sum of proximal and distal resistances for each branch is tuned based on the flow rate in the branches, which assumed to be proportional to the outlet surface areas. The proximal resistances are assumed to be 10% of their corresponding distal resistances. The total resistance is tuned to obtain an average pressure of 100 mmHg for the ascending aorta, a typical physiologic value. The capacitances are tuned to obtain a pressure amplitude between 80–120 mmHg at the outlets. To achieve mesh independence, the mesh is adapted twice based on element residual values [38]. The final mesh contains approximately 2 million tetrahedral elements. A Dirichlet boundary condition is imposed at the inlet, i.e. ascending aorta, with the flow waveform shown in Fig. 10 [37]. All the outlets are constrained for the Lagrange method with a profile order of 5. Also, $\bar{Q}$ in Eq. (20) was tuned to the exact values obtained from the stabilization methods results, giving the Lagrange method an exact initial guess for the flow rates at each outlet.

The flow rate is negative for a significant portion of the cycle for the three upper branches (flow rate plots in Fig. 10), but not for the descending aorta. This backflow results in an unstable solution for the no-treatment case, and the normal constraints case also diverged after 25% of the cardiac cycle.

Since there is no significant flow reversal in the descending aorta, the stabilization method does not have any effect on this outlet. This is also true at flow peak for the other branches, when there is no backflow at these outlets. Comparing the flow traces of the Lagrange and stabilization methods shows no significant difference between the results. Assuming the stabilization method results are close to the supposed no treatment case results, it can be concluded that the Lagrange method does not change the flow split values in this case. This is mainly due to the fact that the flow split is determined by the boundary conditions, rather than the 3D model hemodynamics. This can be simply deduced by comparing the pressure loss through the model to the pressure loss at the boundaries (see Fig. 11).

As seen in this figure, the pressure loss in the model is on the order of 1 mmHg, while the mean pressure imposed by the boundary conditions is approximately 90 mmHg. Since the intrusion of the Lagrange method on the pressure field is of the same order as pressure loss in the model, the

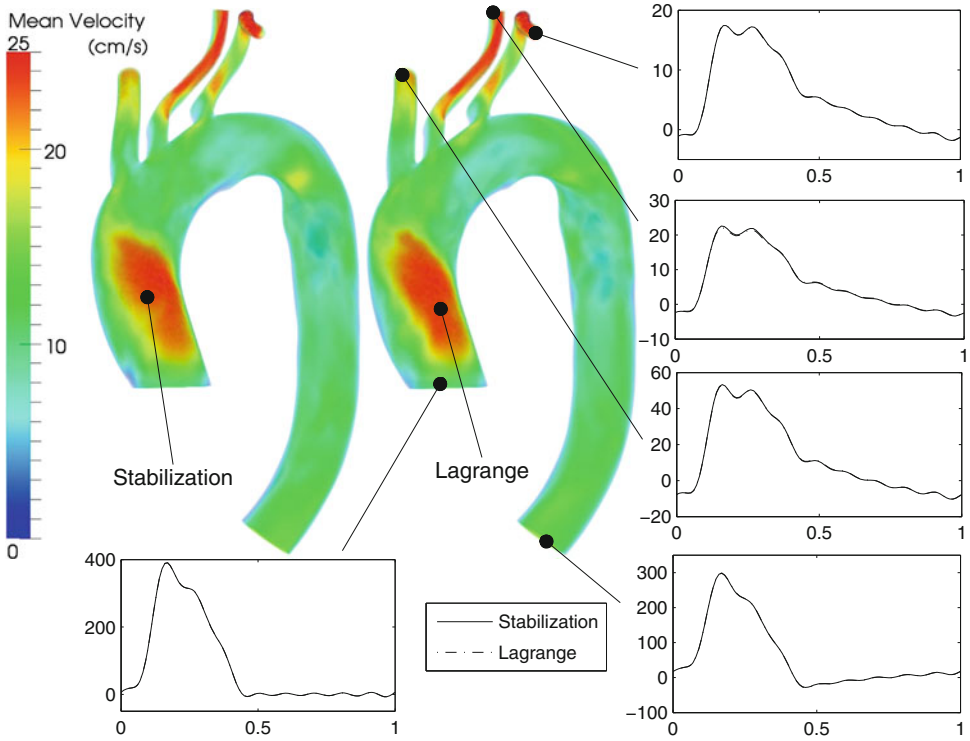

Fig. 10 Flow rates (mL/s versus time) of the outlets obtained from the stabilization and Lagrange methods results. The volumetric contours of time-averaged velocity magnitude are shown for the stabilization and the Lagrange methods

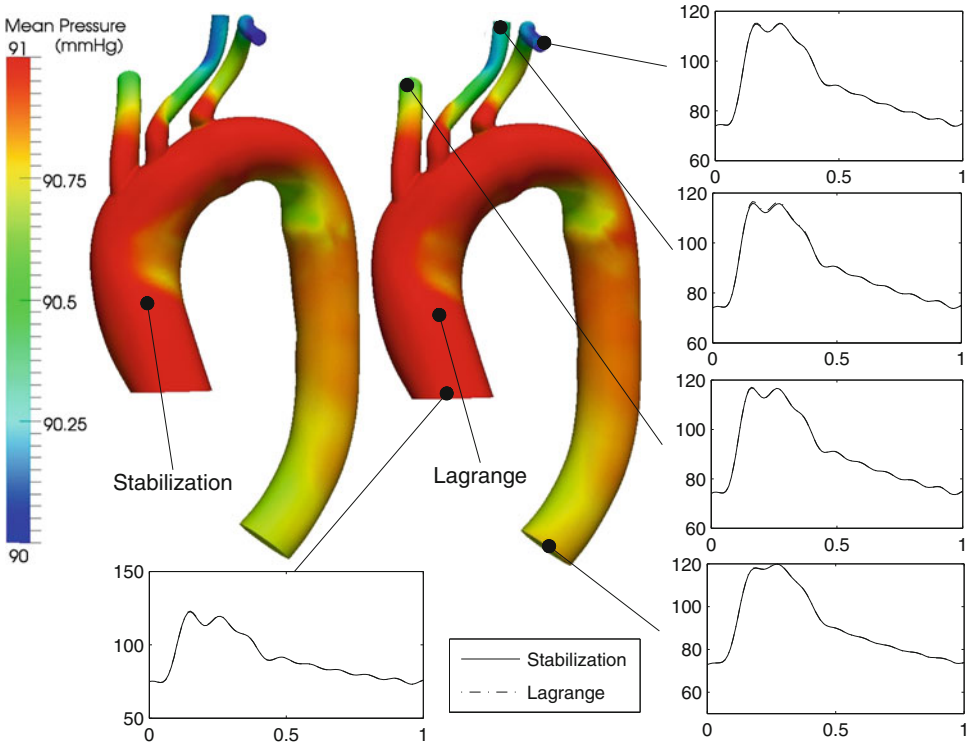

Fig. 11 Pressure plots (mmHg versus time) at the outlets obtained from the Lagrange and stabilization methods. The time-averaged pressure contours at the surface are shown for the stabilization and the Lagrange methods

variation in the pressure field is too small to significantly affect the flow split. Hence, the flow split between the branches is roughly inversely proportional to the sum of distal and proximal resistances.

However, if the Lagrange parameters are not tuned properly, the Lagrange results can be drastically different from the stabilization results. The importance of tuning the Lagrange parameters is deducible from Table 3. The results in this table

Table 3 The effect of tuning Lagrange parameters on the solution

Method	$\bar{Q}_{aoa}$	$\bar{Q}_{aod}$	$\bar{Q}_{ba}$	$\bar{Q}_{lsa}$	$\bar{Q}_{lcca}$	$\bar{P}_{aoa}$	$\bar{P}_{aod}$	$\bar{P}_{ba}$	$\bar{P}_{lsa}$	$\bar{P}_{lcca}$
No-Treatment	−50.0	38.69	7.627	1.411	2.268	14.53	0.0135	0.349	0.331	0.548
Lagrange (I)	−50.0	40.23	7.109	1.788	0.870	15.50	0.7954	2.539	4.390	6.041
Lagrange (II)	−50.0	43.57	5.226	0.860	0.342	13.79	−0.0168	7.147	8.713	9.372
Lagrange (III)	−50.0	46.01	3.191	0.434	0.356	15.21	0.6099	11.54	12.38	10.26

The flow rates are in (mL/s) and pressures are in (Pa). The Lagrange (I) simulation is performed with tuned $\bar{Q}$ obtained from the no-treatment case, and $n = 2$. The Lagrange (II) simulation is performed with tuned $\bar{Q}$ obtained from the no-treatment case, and $n = 5$. The Lagrange (III) is with untuned $\bar{Q}$, and $n = 2$. In this case, $\bar{Q}$ is estimated based on the outlet surface area and aoa flow rate. Note that the stabilization results are identical to the no-treatment case, since there is no backflow at the outlets. *aoa* ascending aorta, *aod* descending aorta, *ba* brachiocephalic artery, *lsa* left subclavian artery, *lcca* left common carotid artery

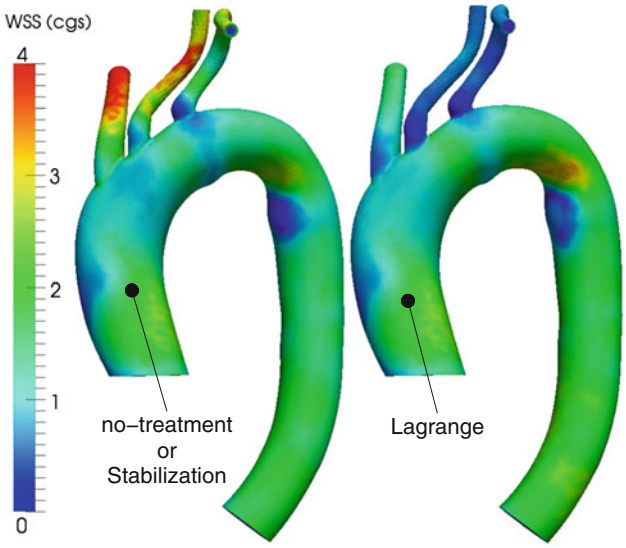

Fig. 12 The wall shear stress contours obtained from the no-treatment and the Lagrange methods results. These results correspond to a steady state, zero traction boundary condition simulation. The $\bar{Q}$ is untuned for the Lagrange method with $n = 2$ (the Lagrange (III) case in Table 3). The Lagrange method predicts lower WSS in the upper branches due to the lower flow rates in these branches. However, the wall shear stress is nearly unaffected for the aortic arch

are obtained from steady state simulations with zero traction boundary conditions for the outlets. In the cases shown, the Lagrange method produces significantly different flow splits compared to the no treatment case, and the difference is made worse if the Lagrange method parameters are not tuned properly (see Table 3).

The contours of wall shear stress magnitude for the steady state case with zero traction boundary conditions are shown in Fig. 12. The Lagrange contours are obtained from the case (III) simulation in Table 3. The changes in the velocity field have caused large changes in the wall shear stress in the upper branches. In these branches the Lagrange method predicts a lower flow rate, and hence a lower wall shear stress. However, in the ascending aorta the wall shear stress predictions are very close, due to the identical flow rates at the inlet.

To illustrate issues with robustness of the proposed methods, we present a case in which we alter the cross sectional

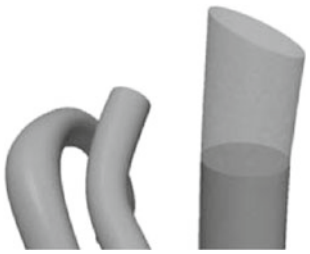

Fig. 13 The brachiocephalic artery with normal and angled cut

cut of one of the model outlets. This represents a situation in which the outlet section cannot be cut perpendicular to the flow direction for reasons related to model construction or lack of image data. Also, due to unsteady flow phenomenon, the primary flow direction at a given outlet can change over the cardiac cycle. Thus, there may be no unique direction for the outlet normal that remains aligned with the flow direction during the entire cycle. The situation is even more challenging when fluid-structure interaction modeling is employed for cardiovascular simulation (see, e.g., [39–42]).

To investigate the robustness of the methods under these non-ideal circumstances, the brachiocephalic outlet is intentionally cut in an off-normal direction to the vessel centerline (see Fig. 13). Therefore, the normal constraint direction is not aligned with the flow direction. Also, the outlet cross section is elliptical, which differs from the assumed circular cross section in Eq. (19). This leads to divergence of the normal constraint simulation after 15% of the cardiac cycle. Compared to the previous case, this demonstrates the sensitivity of the normal constraint method to the outlet cut angle. Without tuning the Lagrange method parameters, the simulation diverges. This is likely a result of inconsistency between the outlet cross section and the assumed cross section in Eq. (19). The stabilization method remains stable for this case, and the time-averaged wall shear stress and pressure contours are smooth, matching well with the previous results. This result indicates improved robustness of the stabilization method in non-ideal circumstances compared to the other two methods.

4 Discussion

The overall performance of the three treatment methods can be compared in terms of robustness, impact on the flow physics, computational cost, implementation effort and ease-of-use aspects.

Comparing the robustness of the three methods used for backflow treatment, the stabilization method performed the best. Robustness was tested by varying the Reynolds number and length of geometry in case study 1, by adding flow pulsatility with backflow in case study 2, and by varying the outlet cut plane in case study 3. For all these cases, the stabilization method produced a numerically stable solution without the need for parameter adjustment. In examining the residuals of the numerical solution, we find that the Lagrange method was stable while the normal constraint method failed for the second and third case studies. However, the residual was still high for the Lagrange method compared to the stabilization method in the second case study, and the obtained solution deviated substantially from the stabilization method results. Both the normal constraint method and the Lagrange method, depending on the formulation, can place additional requirements on the model geometry compared to the stabilization method. The normal constraint method failed faster in case study 3 when the outlet section was not cut properly. Since a circular cross section at the outlets was assumed, the untuned Lagrange method also failed.

Perhaps the most important measure of performance is the impact of the outlet treatment on the flow physics. In this case, the stabilization method outperformed the Lagrange and normal constraint methods. Although the stabilization method can change the pressure slightly due to the added traction, this effect does not appear to be significant, especially when examining the velocity vectors. The stabilization method has absolutely no impact on the flow when there is no backflow. This is also true for the normal constraint if the normal constraint equation is considered only for $\partial_{h\_}\Omega$, i.e. where $U_i^A n_i^A < 0$.

For all cases examined in this work, the Lagrange method had a significant impact on the velocity profile at the constrained outlet. While the effect on the velocity profile shape was restricted to a local region near the outlet, there were important effects on other quantities including pressure and energy loss that propagated globally. Our results showing only local changes in the velocity profile agreed with the previous work of Kim et al. [23]. However, to satisfy the momentum equations, the Lagrange method also resulted in large changes to the pressure at the boundary, which affected the pressure globally throughout the model in case studies 1 and 2. This causes an error in the predicted pressure field in regions far from the constrained boundaries.

Our results suggest that the effect of the Lagrange method on the flow field depends on the type of boundary conditions used. Specifically, the Lagrange results were more accurate when physiologic non-zero traction boundary conditions are used, as compared to the zero traction boundary conditions. When using RCR boundary conditions in case study 3, the pressure changes due to the Lagrange constraint were small compared to the overall mean pressures imposed by the boundary conditions, and therefore, the resulting changes in both flow rate and pressure were not significant. However, the excellent agreement obtained with the Lagrange method for this case required tuning the $\bar{Q}$ values using the stabilization results, and the results were highly variable without tuning. These results also suggest that the Lagrange method may be less suited to problems with lower overall mean pressure, such as venous flow simulations. Decreasing the penalty numbers can decrease the impact of the Lagrange method on the flow physics, but it will also decrease the robustness of this method.

Comparing the results for computational cost, the normal constraint and stabilization methods do not add any significant additional cost, whereas, the Lagrange method can add up to 50% to the computational cost, depending on the problem. This increased cost is due to the additional elements inside the solution vector, i.e. Lagrange multipliers, as well as added blocks inside the stiffness matrix.

The implementation effort required for the normal constraint and stabilization methods are both minimal, because the structure of the stiffness matrix and the linear solver need not be modified for either method. The implementation of the normal constraint method requires somewhat more effort because the rotation matrix must be formed for each element, and also specific blocks of the element stiffness matrix and residual vector should be modified. Due to the new entries in the solution vectors and the changes in the structure of the tangent matrix, the Lagrange method requires the highest implementation effort.

Considering the ease-of-use aspect, the normal constraint and stabilization methods are fairly simple to use. However, the Lagrange method requires the use of several user-defined parameters. For example, the quantity $\bar{Q}$ in Eq. (20) must be estimated and specified by the user prior to the running the simulation, while this parameter should be a simulation result. In practice, this may required a time-intensive iterative procedure. It should be noted that drastic changes in these parameters can have profound effect on the final simulation results, even with RCR boundary conditions.

5 Conclusions

In this work, we have performed a quantitative comparison of three outlet treatment methods used to address the problem of numerical divergence due to backflow. Using identical numerics, models, and meshes, we compared the methods of

outlet stabilization, normal velocity constraint, and Lagrange profile constraints. We have shown that the normal constraint can be safely used in the case of slight flow reversal, producing a stable result with little impact on the flow physics. However, this requires the constrained direction vector to be close to the direction of reversed flow and that only the part of the outlet with flow reversal be constrained.

Our results showed that the Lagrange method, while often successful in stabilizing the solution, suffered from high impact on the pressure field solution, high computational cost, and increased difficulty in both implementation and ease-of-use. While results with highly tuned outlet flows matched very well with the stabilized method results, a lack of tuning can produce drastically different results that are not confined to the vicinity of the outlet.

The stabilization method was shown to have the highest robustness, and the least impact on the flow field, with no extra computational cost, and high ease of implementation and use. In addition, the stability of this method is improved to include a wider range of time steps by adding only a fraction of the convection term in our formulation. This implementation also reduced the impact of this method on the pressure field.

To summarize, the addition of an outlet stabilization term provides an accurate, robust, and easy-to-use method that reliably prevents backflow divergence in numerical simulations of blood flow. Future work will explore the use of these methods for fully coupled multiscale modeling simulations, which require frequent exchange of information between 0D and 3D solutions.

Acknowledgments This work was supported by a Leducq Foundation Network of Excellence Grant, a Burroughs Wellcome Fund Career Award at the Scientific Interface, and an INRIA associated team program. We gratefully acknowledge the use of software from the Simvascular open source project through Simbios (http://simtk.org), as well as the expertise of Dr. Nathan Wilson. The authors gratefully acknowledge Dr. Hyun Jin Kim for her help regarding the Lagrange method coding and implementation.

References

1. Bove EL, Migliavacca F, de Leval MR, Balossino R, Pennati G, Lloyd TR, Khambadkone S, Hsia TY, Dubini G (2008) Use of mathematic modeling to compare and predict hemodynamic effects of the modified blalock-taussig and right ventricle-pulmonary artery shunts for hypoplastic left heart syndrome. J Thorac Cardiovasc Surg 136(2):312–320.e2
2. Migliavacca F, Balossino R, Pennati G, Dubini G, Hsia TY, de Leval MR, Bove EL (2006) Multiscale modelling in biofluidynamics: application to reconstructive paediatric cardiac surgery. J Biomech 39(6):1010–1020
3. Lagana K, Dubini G, Migliavacca F, Pietrabissa R, Pennati G, Veneziani A, Quarteroni A (2002) Multiscale modelling as a tool to prescribe realistic boundary conditions for the study of surgical procedures. Biorheology 39:359–364
4. Urquiza SA, Blanco PJ, Vnere MJ, Feijo RA (2006) Multidimensional modelling for the carotid artery blood flow. Comput Meth Appl Mech Eng 195(33–36):4002–4017
5. Vignon-Clementel IE, Figueroa CA, Jansen KE, Taylor CA (2006) Outflow boundary conditions for three-dimensional finite element modeling of blood flow and pressure in arteries. Comput Meth Appl Mech Eng 195(29–32):3776–3796
6. Blanco PJ, Feijo RA, Urquiza SA (2007) A unified variational approach for coupling 3d-1d models and its blood flow applications. Comput Meth Appl Mech Eng 196(41–44):4391–4410
7. Heywood JG, Rannacher R, Turek S (1996) Artificial boundaries and flux and pressure conditions for the incompressible Navier–Stokes equations. Int J Numer Methods Fluids 22(5):325–352
8. Formaggia L, Gerbeau JF, Nobile F, Quarteroni A (2002) Numerical treatment of defective boundary conditions for the Navier–Stokes equations. SIAM J Numer Anal 40:376–401
9. Formaggia L, Veneziani A, Vergara C (2008) A new approach to numerical solution of defective boundary valve problems in incompressible fluid dynamics. SIAM J Numer Anal 46(6):2769–2794
10. Taylor CA, Hughes TJR, Zarins CK (1998) Finite element modeling of blood flow in arteries. Comput Methods Appl Mech Eng 158(1–2):155–196
11. Taylor CA, Cheng CP, Espinosa LA, Tang BT, Parker D, Herfkens RJ (2002) In vivo quantification of blood flow and wall shear stress in the human abdominal aorta during lower limb exercise. Ann Biomed Eng 30:402–408
12. Lagan K, Balossino R, Migliavacca F, Pennati G, Bove EL, de Leval MR, Dubini G (2005) Multiscale modeling of the cardiovascular system: application to the study of pulmonary and coronary perfusions in the univentricular circulation. J Biomech 38(5):1129–1141
13. Marsden AL, Vignon-Clementel IE, Chan F, Feinstein JA, Taylor CA (2007) Effects of exercise and respiration on hemodynamic efficiency in CFD simulations of the total cavopulmonary connection. Ann Biomed Eng 35:250–263
14. Pekkan K, Dasi LP, Nourparvar P, Yerneni S, Tobita K, Fogel MA, Keller B, Yoganathan A (2008) In vitro hemodynamic investigation of the embryonic aortic arch at late gestation. J Biomech 41(8):1697–1706
15. Pekkan K, Dur O, Sundareswaran K, Kanter K, Fogel M, Yoganathan A, Undar A (2008) Neonatal aortic arch hemodynamics and perfusion during cardiopulmonary bypass. J Biomech Eng 130(6):061012
16. Tezduyar TE, Ramakrishnan S, Sathe S (2008) Stabilized formulations for incompressible flows with thermal coupling. Int J Numer Methods Fluids 57:1189–1209
17. Tezduyar TE, Takizawa K, Moorman C, Wright S, Christopher J (2010) Space-time finite element computation of complex fluid-structure interactions. Int J Numer Methods Fluids 64:1201–1218
18. de Zelicourt D, Ge L, Wang C, Sotiropoulos F, Gilmanov A, Yoganathan A (2009) Flow simulations in arbitrarily complex cardiovascular anatomies - an unstructured cartesian grid approach. Comput Fluids 38(9):1749–1762
19. Marsden AL, Feinstein JA, Taylor CA (2008) A computational framework for derivative-free optimization of cardiovascular geometries. Comput Methods Appl Mech Eng 197(21–24):1890–1905
20. Borazjani I, Ge L, Sotiropoulos F (2010) High-resolution fluid-structure interaction simulations of flow through a bi-leaflet mechanical heart valve in an anatomic aorta. Ann Biomed Eng 38:326–344
21. Vignon-Clementel IE (2006) A Coupled Multidomain Method for Computational Modeling of Blood Flow. PhD thesis, Stanford
22. Bazilevs Y, Gohean JR, Hughes TJR, Moser RD, Zhang Y (2009) Patient-specific isogeometric fluid-structure interaction analysis of thoracic aortic blood flow due to implantation of the Jarvik 2000

left ventricular assist device. Comput Methods Appl Mech Eng 198(45–46):3534–3550
23. Kim HJ, Figueroa CA, Hughes TJR, Jansen KE, Taylor CA (2009) Augmented lagrangian method for constraining the shape of velocity profiles at outlet boundaries for three-dimensional finite element simulations of blood flow. Comput Meth Appl Mech Eng 198(45–46):3551–3566
24. Brooks AN, Hughes TJR (1982) Streamline upwind/petrov-galerkin formulations for convection dominated flows with particular emphasis on the incompressible Navier–Stokes equations. Comput Methods Appl Mech Eng 32(1–3):199–259
25. Tezduyar TE (2003) Computation of moving boundaries and interfaces and stabilization parameters. Int J Numer Methods Fluids 43(5):555–575
26. Bazilevs Y, Calo VM, Cottrell JA, Hughes TJR, Reali A, Scovazzi G (2007) Variational multiscale residual-based turbulence modeling for large eddy simulation of incompressible flows. Comput Methods Appl Mech Eng 197(1–4):173–201
27. Whiting CH, Jansen KE (2001) A stabilized finite element method for the incompressible Navier–Stokes equations using a hierarchical basis. Int J Numer Methods Fluids 35(1):93–116
28. Franca LP, Frey SL (1992) Stabilized finite element methods: II. the incompressible Navier–Stokes equations. Comput Methods Appl Mech Eng 99(2–3):209–233
29. Tezduyar TE, Mittal S, Ray SE, Shih R (1992) Incompressible flow computations with stabilized bilinear and linear equal-order-interpolation velocity–pressure elements. Comput Methods Appl Mech Eng 95:221–242
30. Jansen KE, Whiting CH, Hulbert GM (2000) A generalized-[alpha] method for integrating the filtered Navier–Stokes equations with a stabilized finite element method. Comput Methods Appl Mech Eng 190(3–4):305–319
31. Shakib F, Hughes TJR, Johan Z (1989) A multi-element group preconditioned gmres algorithm for nonsymmetric systems arising in finite element analysis. Comput Methods Appl Mech Eng 75(1–3):415–456
32. Gresho PM, Sani RL (2000) Incompressible flow and the finite element method, vol 2. Wiley
33. Schmidt JP, Delp SL, Sherman MA, Taylor CA, Pande VS, Altman RB (2008) The Simbios National Center: systems biology in motion. In: Proceedings of the IEEE, vol 96, issue 8, pp 1266–1280
34. Vignon-Clementel IE, Marsden AL, Feinstein JA (2010) A primer on computational simulation in congenital heart disease for the clinician. Progress Pediatr Cardiol 30(1–2):3–13
35. Vignon-Clementel IE, Figueroa CA, Jansen KE, Taylor CA (2010) Outflow boundary conditions for three-dimensional simulations of non-periodic blood flow and pressure fields in deformable arteries. Comput Methods Biomech Biomed Eng 13(5):625–640
36. Migliavacca F, Pennati G, Dubini G, Fumero R, Pietrabissa R, Urcelay G, Bove EL, Hsia TY, De Leval MR (2001) Modeling of the norwood circulation: effects of shunt size, vascular resistances, and heart rate. Am J Physiol Heart Circ Physiol 280:H2076–H2086
37. Kim H, Vignon-Clementel IE, Coogan J, Figueroa C, Jansen KE, Taylor CA (2010) Patient-specific modeling of blood flow and pressure in human coronary arteries. Ann Biomed Eng 38:3195–3209
38. Sahni O, Muller J, Jansen KE, Shephard MS, Taylor CA (2006) Efficient anisotropic adaptive discretization of the cardiovascular system. Comput Methods Appl Mech Eng 195(41–43):5634–5655
39. Bazilevs Y, Calo VM, Zhang Y, Hughes TJR (2006) Isogeometric fluid-structure interaction analysis with applications to arterial blood flow. Comput Mech 38:310–322
40. Bazilevs Y, Calo VM, Hughes TJR, Zhang Y (2008) Isogeometric fluid-structure interaction: theory, algorithms, and computations. Comput Mech 43:3–37
41. Takizawa K, Moorman C, Wright S, Purdue J, McPhail T, Chen PR, Warren J, Tezduyar TE (2011) Patient-specific arterial fluid-structure interaction modeling of cerebral aneurysms. Int J Numer Methods Fluids 65:308–323
42. Tezduyar TE, Takizawa K, Brummer T, Chen PR (2011) Space–time fluid–structure interaction modeling of patient-specific cerebral aneurysms. Int J Numer Methods Biomed Eng 27. doi:10.1002/cnm.1433